Acta Materialia 268 (2024) 119748

Contents lists available at ScienceDirect

Acta Materialia

journal homepage: www.elsevier.com/locate/actamat

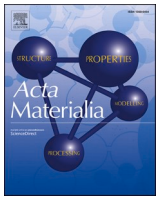

Topology and evolution of dislocation structures mediated by glissile reactions in face-centered cubic metals

Fulin Wang [a,*], Jinjin Guo [b], Daniel Weygand [c], Fenghua Wang [a], Timothy J. Rupert [d], Dengke Chen [b,*], Daniel S. Gianola [e,*]

[a] National Engineering Research Center of Light Alloy Net Forming and State Key Laboratory of Metal Matrix Composite, School of Materials Science and Engineering, Shanghai Jiao Tong University, Shanghai 200240, China
[b] Department of Engineering Mechanics, School of Naval Architecture, Ocean and Civil Engineering, Shanghai Jiao Tong University, Shanghai 200240, China
[c] Institute for Applied Materials, Karlsruhe Institute of Technology, Karlsruhe 76131, Germany
[d] Department of Materials Science and Engineering, University of California Irvine, Irvine, CA 92697, USA
[e] Materials Department, University of California Santa Barbara, Santa Barbara, CA 93106, USA

ARTICLE INFO

Keywords:
Dislocation structure
Hardening
Transmission electron microscopy
Discrete dislocation dynamics
3D characterization

ABSTRACT

The strength and hardening of metallic materials are dictated by the motion and interactions of dislocations. Individual dislocations intersect, react, and frequently form junctions, defining a defect topology that is the basis of subsequent deformation. While immobilized dislocation locks are intuitively considered as potent strengthening structures, simulations suggest that glissile reactions are a predominant contributor to hardening among the four types of dislocation reactions in face-centered cubic crystals, even though the resulting dislocations are inherently mobile. To date, the prevailing understanding of glissile reactions has been primarily based on classical geometric models of perfect dislocations and simulations thereof. Understandings of the reaction pathways and detailed experimental characterization of glissile reactions are lacking, leaving the potential topological variations shrouded in mystery. This study details molecular dynamics simulations of glissile reaction involving dissociated partial dislocations, and the direct experimental characterization of the dislocation configurations resulting from glissile reactions in deformed pure aluminum using transmission electron microscopy. The experimentally-determined structure was reconstructed in 3D and parametrically studied in discrete dislocation dynamics simulations, revealing varying topological evolutions under different loading conditions. Further statistical analyses on an ensemble of simulated dislocations revealed the essential role of stress states and cross-slip in affecting the probability of glissile reaction and the fraction of mobile dislocation nodes. These findings point to avenues for the development of dislocation-based constitutive theories of plasticity.

1. Introduction

Linear defects in a crystalline solid, known as dislocations, are the vehicles for plastic deformation and underpin the competing requirements of high performing structural materials. Inhibiting their otherwise facile motion by engineering obstacles on crystallographic slip planes provides the means for strengthening. However, the complex nature of dislocations acting in an ensemble during plastic deformation and their ensuing evolution in both density and topology are currently gaps in our understanding and act to limit the predictive power of existing plastic deformation models.

Dislocations interact with other dislocations (and other microstructural features such as solute atoms and precipitates) via their elastic field and can react with each other, with products defined by the defect topology. The resulting junctions are commonly thought of as immobilized sites for the interacting dislocation segments. The junctions thereby also increase the resistance to further glide of the dislocations pinned at the reaction nodes. Indeed, conventional wisdom suggests that immobilizing these junctions provides the means for strengthening. Based on the crystallography of the interacting slip systems, dislocation reactions in metals adopting a face-centered cubic (FCC) crystal structure are categorized into four types: (i) Hirth locks, (ii) Lomer locks formed by perfect dislocations (and Lomer–Cottrell locks formed by partial dislocations), (iii) collinear reactions, and (iv) glissile reactions,

* Corresponding authors.
E-mail addresses: fulinwang@sjtu.edu.cn (F. Wang), dengke.chen@sjtu.edu.cn (D. Chen), gianola@ucsb.edu (D.S. Gianola).

https://doi.org/10.1016/j.actamat.2024.119748
Received 13 September 2023; Received in revised form 7 February 2024; Accepted 8 February 2024
Available online 8 February 2024

defined as a reaction leading to glissile (mobile) products [1]. The former two are straightforward dislocation locks that immobilize the intersecting dislocations, whereas the latter two are expected to exhibit a range of structural evolution.

The prevailing knowledge of dislocation reactions, the evolution of their products, and more importantly their effect on plastic deformation have been primarily based on classical geometric models and corresponding simulations of such configurations. For instance, using atomic-scale and continuum models of plasticity [2], collinear reactions in FCC crystals were evaluated as the most potent strengtheners among all the dislocation reactions. Mechanistically, this phenomenon was ascribed to the fact that the resulting dislocations are perfectly glissile. When two dislocations of the same Burgers vector (referred to as collinear dislocations), yet gliding on two {111} planes, intersect, dislocation annihilation along the intersection lines occurs such that the reacting dislocations change their glide planes at the nodes, producing two nodes that are constrained to follow the intersection line of the two participating glide planes. These results highlight that the interactions of glissile dislocations can result in mobile junctions that contribute to the strain hardening of crystals, in addition to immobile (sessile) dislocation junctions.

Recent evidence suggests that not only can such mobile dislocation junctions form via a glissile reaction, but also that the glissile junctions are the predominant contributor to strain hardening once plastic flow ensues. When two dislocations with different $1/2\langle 110\rangle$ Burgers vectors and gliding on two {111} planes intersect, the Burgers vector of the resulting dislocation is also of $1/2\langle 110\rangle$ type, and, very importantly, lies on one of the initial two {111} planes (Fig. 1). A convenient formula defining a glissile reaction is $b_1^\alpha + b_2^\beta = b_3^\beta$, where b is the $1/2\langle 110\rangle$ type Burgers vector and the superscript α and β denote two different {111} slip planes. Since the reacting and resulting dislocations are on their respective slip planes, all the three dislocation segments connected to the joining node are glissile. This is distinct from a Lomer lock, where the resulting Burgers vector is a $1/2\langle 110\rangle$ type, but the dislocation line direction and Burgers vector are not on the same {111} plane, so the resulting junction is immobile.

Despite the knowledge of glissile junctions as one possible reaction in FCC crystals (with its name implying mobility), their crucial role in mediating multiplication mechanisms that evolve the dislocation density and contribute to hardening has only recently attracted interest from the materials modelling community. Discrete dislocation dynamics (DDD) simulations have demonstrated that, on the one hand, glissile reactions are an effective source for generating mobile dislocations, especially on new slip systems, thereby contributing to the multiplicity of plastic deformation modes [3–5]. This observation further questions the Frank–Read theory for dislocation multiplication within entangled dislocation networks. On the other hand, glissile reactions were demonstrated to be the dominant contributor to hardening [6], owing to the high probability of intersections of appropriate dislocation species [2,7] and the formation of stable junctions [6]. Taken as a whole, the dual nature of junction mobility underscores the role of glissile reactions in both providing mobile dislocations as carriers of plastic strain and producing immobile structures as obstacles for dislocation movement. It is noteworthy that, very recently, glissile junction formation was added to a dislocation density-based crystal plasticity model [8].

The seminal work on dislocation reactions by Whelan [9] (originally referred to as "case 2. Burgers vectors at 120°"), where planar hexagonal arrays were observed, led to the authors inferring glissile reactions as a mechanism to generate the dislocation arrays. However, the dislocation Burgers vectors and line directions were not explicitly characterized in the TEM images. To date, and to the best of our knowledge, detailed experimental characterization of a glissile junction has been absent. This is presumably due to the evolving nature of all the mobile dislocations involved in the reaction, thereby demanding challenging and spatially-resolved electron microscopy that characterizes the full 3D elements of each dislocation segment. Note that for the schematic drawing in Fig. 1, distinguishing a glissile reaction from a Lomer lock requires determining the exact Burgers vectors and also the line directions of the dislocations. The lack of detailed experimental characterization leaves any potential structural variations of glissile reactions unknown. Furthermore, predictive models for strength and plastic flow stand to benefit from the knowledge of the actual existence of such junctions under experimental conditions, and how their configuration responds to the diversity of local conditions present in deformed materials. Aiming at determining material-dependent hardening parameters, Madec and Kubin [10] have used dislocation dynamics simulations to calculate the strengthening coefficient of various junctions, including glissile junctions. As a first order of approximation, the line direction of the junction segment was assumed to remain along the intersection line of the slip planes, even though the glissile junction is crystallographically mobile. Interestingly, recent DDD simulations [5] showed that a sequence of dislocation reactions acting in concert, namely a coplanar reaction following a glissile reaction, led to dislocation multiplication on unstressed slip systems, a phenomenon termed slip-free multiplication. These recent simulation results highlight that the impact of glissile reactions on plastic deformation and their impact on engineering properties is yet to be fully elucidated.

The present study firstly examines the reaction pathway of glissile reaction using molecular dynamics (MD) simulations, where dissociated dislocations are considered. This is complementary to the current state of understanding based on perfect dislocations, such as the schematic drawing in Fig. 1. The direct experimental characterization of the dislocation configuration resulting from glissile reactions in deformed pure Al is then detailed using transmission electron microscopy (TEM). All of the characteristic vectors of each dislocation are precisely determined, allowing us to transfer the experimentally determined configuration to DDD simulations to parametrically study its evolution under a variety of loading conditions. Motivated by the observations that the end-nodes of glissile reactions exhibit different states, namely mobile or pinned, we further generalized the findings to an ensemble of dislocations in DDD simulations. The combination of experimental and simulation studies on isolated dislocation junctions and dislocation ensemble helps unravel the interplay of collective mechanisms across scales, analogous to multiscale studies of grain boundary phenomena on bi-

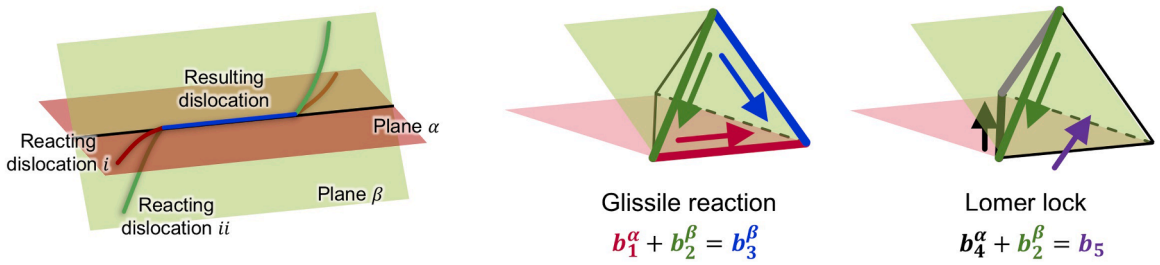

Fig. 1. Definition of glissile reaction and its distinction from a Lomer lock. The Burgers vectors are of $1/2\langle 110\rangle$ type and the two slip planes are {111} type. A Thompson tetrahedron is used to depict the relationships between the planes and Burgers vectors.

crystals ("tame") and polycrystal networks ("in the wild") [11,12]. Altogether, the direct integration of experimental quantification and simulation reveals substantial variabilities of glissile reaction in FCC metals, in terms of both the probability of occurrence and the mobility of the resulting dislocation nodes and their behaviors under load.

2. Methods

2.1. Molecular dynamics simulations

MD simulations were carried out to study the reaction process of glissile reaction. Since the separation distance between the dissociated partial dislocations is proportional to μ/γ_{SF}, where μ is the shear modulus, and γ_{SF} is the stacking fault (SF) energy, two model materials, Cu and Al, are adopted to represent the cases of wide and narrow dislocation dissociation respectively (Al: $\mu/\gamma_{SF} = 0.19$, and Cu: $\mu/\gamma_{SF} = 0.91$). Fig. 2 shows the detailed atomic configuration of simulation setup. The simulation cell has the dimension of 21 nm $\times$ 32 nm $\times$ 55 nm and contains a total of $\sim 2,800,000$ atoms. Simulations were performed using LAMMPS [13] at temperature of 0 K. The embedded atom method (EAM) potentials of Cu by Mishin et al. [14] and of Al by Angelo et al. [15] were employed. The visualization tool OVITO [16] was employed to perform common neighbor analysis to clearly display the dislocation core structure. Two parallel dislocations are generated on the glide planes of *ABC* and *BCD* (Fig. 2(A)), the Burgers vectors are *CA* and *BC* respectively and the line direction is along *BC*. The perfect dislocations dissociated into partial dislocations with SFs in between (Fig. 2(B)), and the ends of the dislocations are fixed at the surface to observe the intermediate process of the reaction. After the dislocations are generated, the energy of system is minimized by conjugate gradient method.

2.2. TEM characterization of dislocations

A commercially pure FCC polycrystalline Al alloy was subjected to moderate plastic deformation (3 % global strain) in uniaxial tension at room temperature to introduce a population of dislocations and facilitate their interactions. TEM specimens with areas of electron transparency were prepared from the bulk by mechanical grinding, rim-punching and electro-polishing. Dislocations were characterized using two-beam diffraction contrast imaging performed on an FEI Tecnai G2 operating at 200 kV using a double tilt specimen holder. For each diffraction condition, the tilt angles of the holder $(\alpha,\ \beta)$ were recorded and used to calculate the relevant crystallographic orientations. Dislocation Burgers vector was determined using the $g{\cdot}b = 0$ invisibility criterion.

For dislocation line direction determination, there are two major methods: dislocation tomography and stereo-pair analyses. The former is based on the concept of reconstructing a 3-D volume by serial 2-D sections, which are acquired as elaborate tilt series images that cover a large tilting range (e.g. $\pm 70^{\circ}$) at small tilt intervals (e.g. 1°) [17–19]. The latter is based on the perspective views of 3-D objects from two distinct directions (therefore the attractive notion of quantifying 3D structure from only two images). The post-acquisition 3-D reconstruction is carried out by the principles of either (1) the projection geometry of line lengths as a function of the tilt and depth of objects in a volume [20,21] or (2) plane trace analysis utilizing the relationship of the objects with the known beam direction and diffraction vector in the crystal coordinate system [22]. In the current study, dislocation line direction was determined based on the stereo-pair method, where dislocation segments in the images were approximated by straight lines.

The relationship between the crystal coordinate system and stage coordinate system is firstly established using the double-tilt angles of the stage for two crystallographic zone axes, following the procedures detailed in [23]. This ensures consistent indexing of the crystallographic zone axes and diffraction vectors, and allows the calculation of electron beam direction for each TEM image (e.g. as shown in Fig. 3). Therefore, in an image formed at a two-beam diffraction condition, a dislocation segment i is associated with a pair of crystallographic directions (beam direction, diffraction vector) $= (B_j,\ g_j)$. The former is perpendicular to the image plane, and the latter is in the image plane and is the normal direction of an edge-on plane. In each image, the angle of the dislocation with the diffraction vector and its projected length are measured as θ_{ij} and l_{ij}. The measured angle should be corrected by the rotation between the image plane and the diffraction plane of the microscope. It is then converted to the angle between g_i and the normal direction of the edge-on plane that contains the dislocation in the image θ^n_{ij}, and is reduced to the range of $[-180^{\circ},\ +180^{\circ}]$. The edge-on planes $\boldsymbol{n}_{ij}$ that contain the dislocation segment i now can be determined by

$$\boldsymbol{n}_{ij}{\cdot}\boldsymbol{g}_j = \cos\theta^n_{ij},\ \boldsymbol{n}_{ij}{\cdot}\,\boldsymbol{B}_j = 0,\ sign\left(\boldsymbol{g}_j \times \boldsymbol{n}_{ij}\right) = sign\left(\theta^n_{ij}\right) \tag{1}$$

The dislocation line direction $\boldsymbol{\xi}$ is ultimately determined as the intersection of the two edge-on planes

$$\boldsymbol{\xi}_i = \boldsymbol{n}_{ij} \times \boldsymbol{n}_{ik} \tag{2}$$

According to the principle of projection, the true line length is calculated from the measured projected length in the image as

$$L_i = \frac{l_i}{\left|\boldsymbol{\xi}_i \times \boldsymbol{B}_j\right|} \tag{3}$$

In summary, once the crystal coordinate system has been established and linked to the sample system, the input parameters for line direction determination include the tilt angles of each image $(\alpha_j,\ \beta_j)$, the diffraction vector g_j, the angle θ^n_{ij} between g_j and the edge-on plane n_{ij}

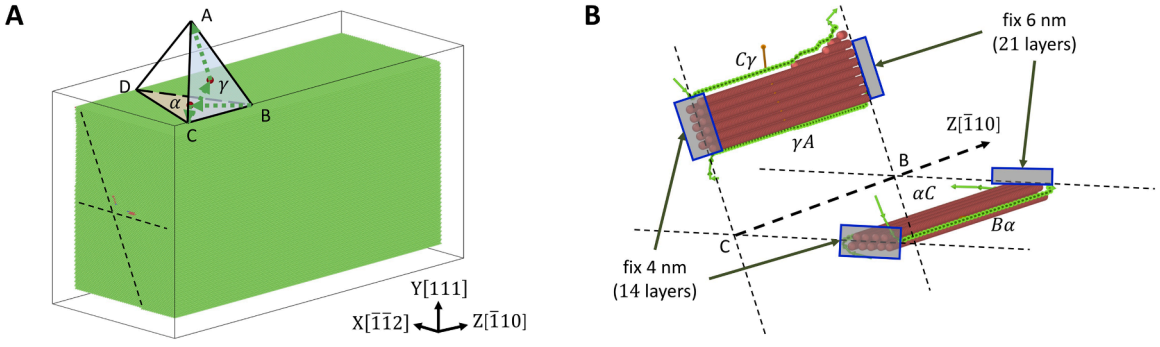

Fig. 2. Atomic configuration for the atomistic simulation. (A) Initial configuration of the simulation cell. OVITO is used for a common neighbor analysis, where atoms with FCC structure (green), and hexagonal-close packed (HCP) structure (red) are differentiated. The surface atoms are removed to show the interior of the simulation cell. The slip planes and the Burgers vector are shown by the Thompson tetrahedron. (B) The core structures of the two partial dislocation pairs and the associated stacking faults. (For interpretation of the references to color in this figure legend, the reader is referred to the web version of this article.)

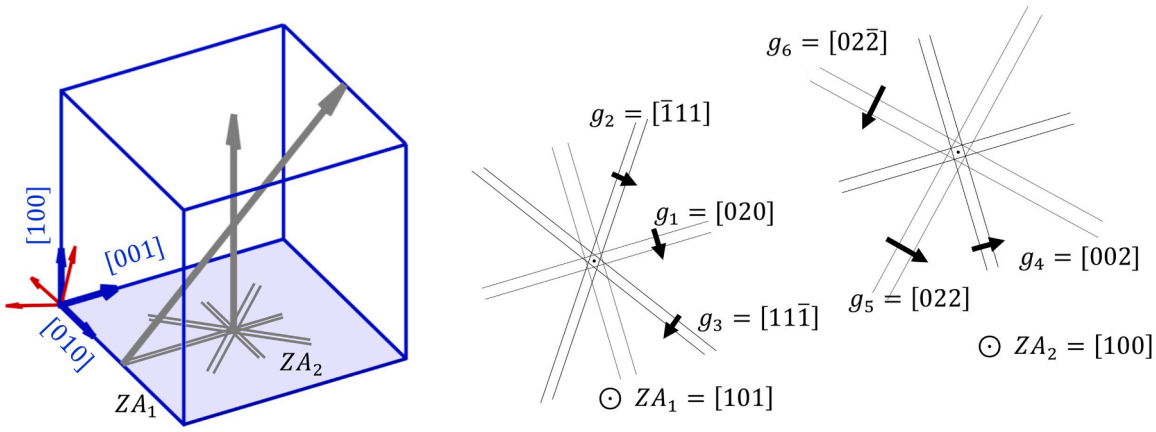

Fig. 3. The crystallographic frame of the investigated grain in the sample. Both the real space crystal and the Kikuchi bands are shown. The coordinate system of the double tilt holder is given as [*XYZ*]. The α and β tilts are with respect to the *X* and *Y* axes respectively, and the signs follow the right-hand rule. The ZA and diffraction vectors are consistently indexed according to the tilt angles on the TEM holder. The positions of the diffraction vector arrows on the Kikuchi bands represent schematically the beam positions.

that contains the dislocation *i*, and the projected length l_{ij}. The results are the dislocation line direction in the crystal coordinate system $\boldsymbol{\xi}_i$ and the true length L_i. Although mathematically two images suffice to determine a straight line in 3-D images, multiple images were employed in the present work to measure and refine each dislocation line segment.

2.3. Simulation of a few dislocations using DDLab

To investigate the possible evolutions of the experimentally-determined dislocation configuration, the experimentally determined dislocations were reconstructed and simulated using the DDLab code [24] that runs in the MATLAB environment. Relevant to aluminum, the elastic constants of shear modulus $G = 27$ GPa and Poisson's ratio $\nu = 0.35$ are used. The dislocation Burgers vector magnitude is set as $b = 0.286$ nm. The damping coefficients for screw and edge dislocations are 10^{-4} Pa s and 0.5×10^{-4} Pa s, respectively, with the ratio of the values set according to [25]. Cross-slip is not allowed in the simulation. A uniaxial load of 200 MPa was applied to the simulation box along different crystallographic directions and the motions of dislocations were tracked as they approached the new equilibrium state.

2.4. Simulation of a large ensemble of dislocations

The DDD framework, as detailed in [3,26-30], is used to simulate the evolution of a large ensemble of dislocations in a single crystal during tensile loading along both [010] and [123] directions, to obtain a statistical understanding. Material parameters for aluminum are used assuming isotropic elastic properties (shear modulus $G = 27$ GPa, Poisson's ratio $\nu = 0.35$, dislocation Burgers vector magnitude $b = 0.286$ nm, friction coefficient $B = 10^{-4}$ Pa s). The simulation sample side length is 5 μm. The tensile test uses displacement-controlled boundary conditions. The bottom surface is fixed, while the displacement in tensile direction at the top surface is prescribed using a strain rate of 2000 s^{-1}. Traction free boundary conditions are prescribed for all remaining degrees of freedom of the surface. Finiteness of the sample is implemented via the superposition principle, which accounts for both boundary conditions and image forces [26,31].

To avoid artificial pinning points in the dislocation structure, the initial structure is obtained by a relaxation scheme [32], which is applied to a dislocation structure starting from randomly distributed circular dislocation loops. The loop radii are comprised between 0.5 and 2 of the sample side length, thus many loops of the initial structure already intersect the surface. The relaxation is performed under traction free boundary conditions and convergence is reached once the dislocation density stabilizes. All dislocation reactions are allowed to occur during relaxation. The dislocation topology evolution due to junction formation, cross-slip and annihilation are treated with constitutive rules [26,33]. The relaxed structure's density is about one fifth of the initial one. Identical relaxed initial dislocation structures are used for the tensile tests with and without cross-slip. The cross-slip formulation [34] and parameters from [35] are used with the proposed parameters for Al, $\text{tau}_{III} = 5$ MPa, to increase the cross-slip probability, the critical distance between screw dislocation $y_s = 1$ μm, and the activation volume is kept at $V = 300b^3$ (*b* is the magnitude of Burgers vector). The role of cross-slip is thus studied in a generic way, meaning a FCC material with easy cross-slip and without cross-slip.

3. Results and discussion

3.1. MD simulations of glissile reaction pathways from dissociated dislocations and their evolution

The occurrence of glissile reactions was examined by allowing the instantiated dissociated dislocations to naturally evolve when the simulation box is relaxed, with the ends of the dislocations pinned (Fig. 4). This configuration represents the reaction of two dislocations with the Burgers vectors of *AC* and *BC*, and on their glide planes *ACB* and *DCB*, respectively. Driven solely by the internal elastic interactions of the dislocations, it was observed that the two partial dislocation pairs glide toward each other. The leading partial γA on the *ACB* plane passes across the plane intersection, and the trailing partial $C\gamma$ reacts with the leading partial αC on the *BCD* plane (Fig. 4(B)), forming a junction with Burgers vector $\alpha\gamma$, i.e. $\alpha C + C\gamma = \alpha\gamma$. This partial dislocation junction is a stair-rod, so it is sessile and remains on the intersection line of the two glide planes. When the trailing partial $B\alpha$ arrives at the intersection line, it reacts with the stair-rod $\alpha\gamma$ (Fig. 4(C)), resulting in $B\gamma$, i.e. $B\alpha + \alpha\gamma = B\gamma$.

The sequential reactions of the partial dislocation pairs occur naturally under zero applied stress. More significantly, this is the only way the reaction could occur, as other combinations of the partial dislocations are energetically less favorable. While the reaction pathway involving partial dislocations is clarified, it is noteworthy that the overall Burgers vectors are consistent with the classical definition using perfect dislocations. After the reaction, the summation of the peripheral partials on the *ACB* plane is $C\gamma + \gamma A = CA$, the summation of the peripheral partials on the *DCB* plane is $B\alpha + \alpha C = BC$, and the summation of the central partials is $B\gamma + \gamma A = BA$. In other words, the intersection and reaction of *CA* and *BC* produces *BA*. The fine structure that the

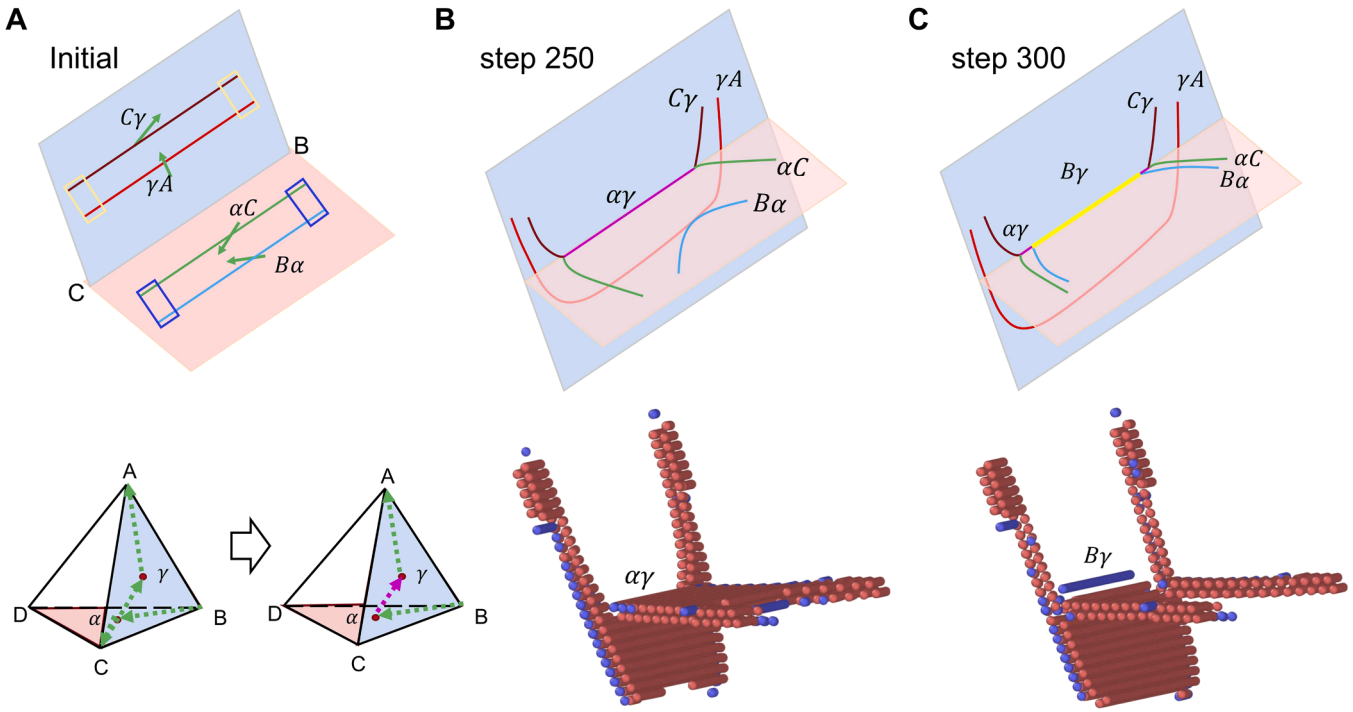

Fig. 4. Dislocation configurations extracted from the atomic snapshots of MD simulations at (A) the initial state, (B) 250 and (C) 300 simulation steps. The partial dislocations are pinned at their ends at the initial state. The Thompson's tetrahedron shows the relevant Burgers vectors and slip planes. The inclined *ABC* plane is colored as blue, and the base *BCD* plane is colored as red.(For interpretation of the references to color in this figure legend, the reader is referred to the web version of this article.)

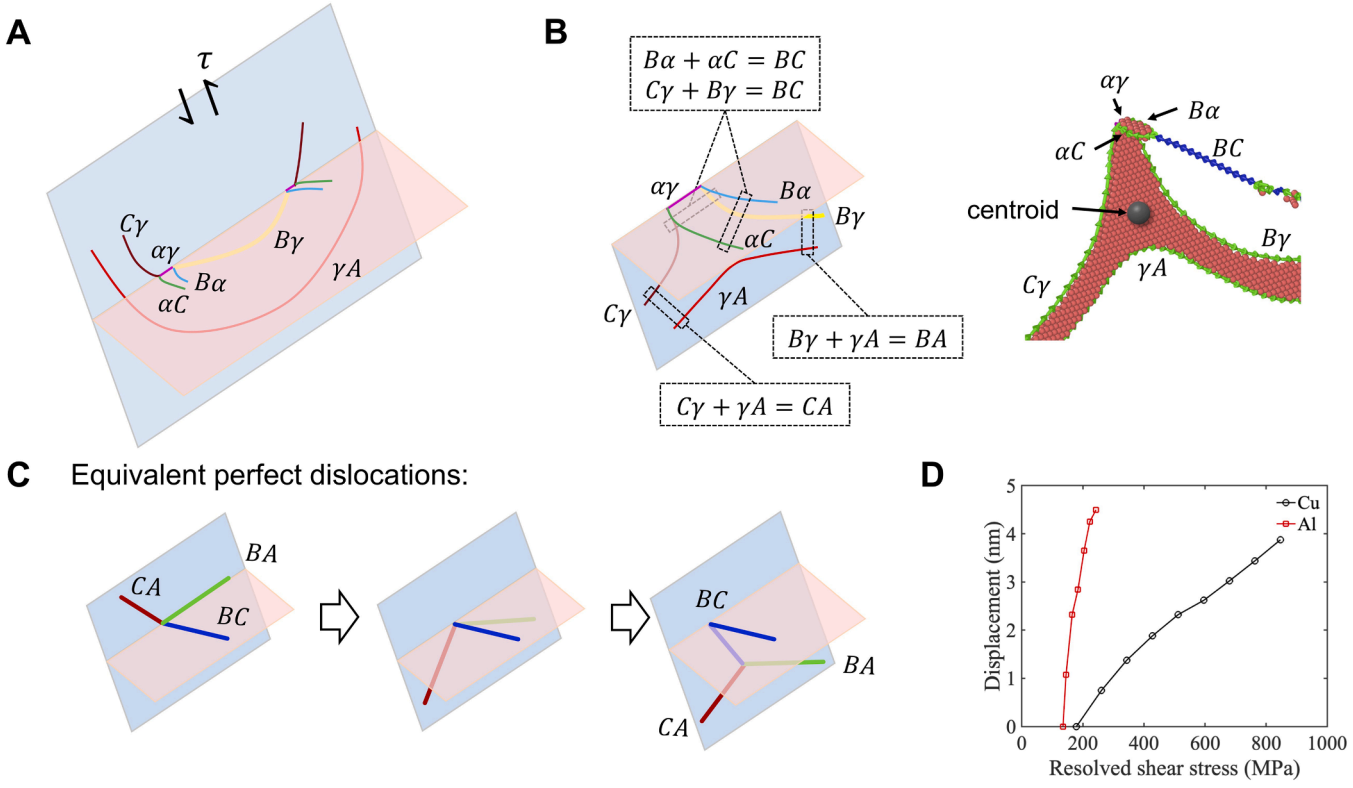

Fig. 5. (A) Slight bowing of the configuration resulting from glissile reaction under a shear stress on the inclined slip plane. (B) Evolved configuration around the left node in (A). The dashed line boxes indicate the equivalent Burgers vectors of perfect dislocations. The atomic configuration corresponding to Al is shown on the right, with the centroid of the three joining stripes of SFs annotated. (C) The evolution of the dislocations around the left node in (A) in terms of the equivalent perfect dislocations from (A) to (B). (D) The change of the displacement of the centroid, as indicated in (B), with increasing RSS on the plane for Cu and Al.

atomistic simulations, which incorporate partial dislocation reactions, reveals is the existence of sessile stair-rods $\alpha\gamma$ at the left and right nodes and along the intersection line. Different stacking fault energies change the separation distance of the partial pairs, but does not appear to significantly affect the reaction process. From the perspective of perfect dislocations, the node joined by three glissile perfect dislocations are expected to be mobile, as shown in the schematic drawing in Fig. 1. From the perspective of partial dislocations, the mobility of the node hinges on the subsequent evolution of the structure surrounding the sessile segment $\alpha\gamma$. At least, the glissile reaction node is expected to be mobile along the intersection line of the two glide planes.

Once the reaction has completed, a displacement field is next applied to the simulation volume to produce a shear stress on the *ABC* plane and perpendicular to the intersection line (Fig. 5(A)). While all the dislocations on the inclined *ABD* plane were driven to glide, the evolution of the structure was tracked, with a focus on the partial dislocations around the stair-rod. It is observed that both the pair of $C\gamma - \gamma A$ and the pair of $B\gamma - \gamma A$ gradually glide below the intersection line of the two glide planes, with $B\gamma$ bowing between the pinned stair-rod segments, while the pair of $\alpha C - B\alpha$ remains on the *BCD* plane (Fig. 5(B)). With further straining, the partials $C\gamma$ and $B\gamma$ get closer, ultimately forming a fourth partial pair on the *ABC* plane. Considering the equivalent perfect dislocations of the structures in Fig. 5(A) and (B), the evolution can be understood as the gliding of *CA* and *BA* on plane *ABC*, followed by the zipping of *CA* and *BA* that produces *BC* on the *ABC* plane, as illustrated in Fig. 5(C). The significance of this process is that a co-planar configuration of three dislocations is created, thereby increasing the degree of freedom of the node from linear motion (1D) along the intersection line to planar motion (2D).

Indeed, the structure of three joining stripes of SFs on the *ABC* plane, which can be approximated as a node joined by three perfect dislocations, is mobile. For Al, a high stacking fault energy material that represents narrow partial separation, the sessile stair-rod $\alpha\gamma$ can be removed when the pairs of $\alpha C - B\alpha$ and $C\gamma - B\gamma$ are stressed to glide closer and therefore unzip the junction of $\alpha\gamma$. For Cu that represents wide partial separation, the junction of $\alpha\gamma$ remains, and all the SFs are wider than Al. The centroid of the three joining stripes of SFs is taken as a reference point to track its equilibrium position with increasing resolved shear stress, which is shown for both Al and Cu in Fig. 5(D). For the same amount of displacement, the RSS increment for Cu is about 9 times that for Al. This result implies that for materials with low SF energy, the node of glissile reaction can be more easily mobilized under an applied stress, via the formation of a co-planar configuration and glide thereafter, whereas for materials with high SF energy, the node is less mobile or acts essentially as pinned. Other initial conditions of parent dislocations (e.g. with different inclinations rather than being parallel) may also influence the difficulty of the junction to remobilize. Again, the presence of the immobile stair-rod segment arises only from the partial reactions, and would otherwise not be predicted using full dislocation models alone.

3.2. Experimental characterization of a structure of glissile dislocations

The MD simulations above elucidated the natural occurrence of a glissile reaction from the perspective of dissociated partial dislocations, and the ability of the involved dislocations and nodes to move under an applied stress, especially for the case of low SF energy materials. We next focused on experimentally identifying and characterizing a dislocation junction structure. Such a dislocation structure, residing in a grain

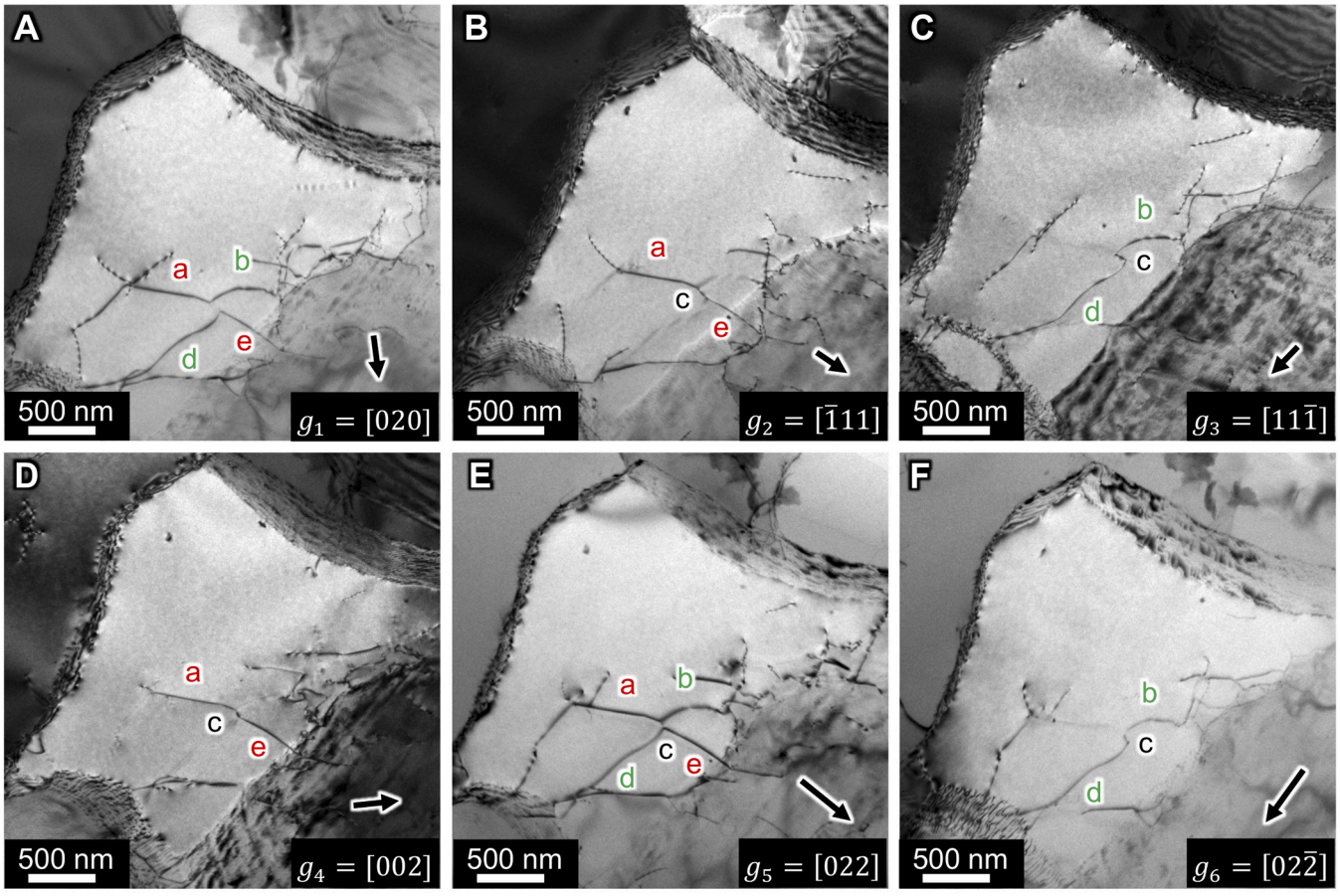

Fig. 6. Five dislocation segments joining at two nodes in a grain of deformed Al. The dislocation segments are indicated by *a, b, c, d* and *e*. The same dislocations are imaged at six diffraction conditions (A–F). The diffraction vector, *g*, is annotated in each image and its direction is indicated by an arrow.

interior in deformed polycrystalline Al specimen, is shown in the TEM two-beam bright field images in Fig. 6. The same set of dislocations were imaged using six different diffraction vectors $\boldsymbol{g}_i$ (Fig. 6(A)–(E)), exhibiting different visibilities. At the diffraction condition of $\boldsymbol{g}_5 = [022]$ (Fig. 6(E)), all five dislocations (denoted by the letters *a*-*e*) are visible. Dislocation *c* is joined by dislocations *a* and *b* at one node and by dislocations *d* and *e* at another node, thereby comprising a typical binary junction. Using the $\boldsymbol{g}\cdot\boldsymbol{b} = 0$ invisibility criterion where specific combinations of diffraction vectors used for imaging, $\boldsymbol{g}$, and Burgers vector, $\boldsymbol{b}$, result in zero or weak contrast, the Burgers vectors of the five individual dislocations were determined (Table 1). Dislocations *a* and *e* have the same Burgers vector of $\boldsymbol{b}_{a,e} = 1/2[011]$, dislocations *b* and *d* have a different Burgers vector of $\boldsymbol{b}_{b,d} = 1/2[110]$, and the Burgers vector of dislocation *c* is $\boldsymbol{b}_c = 1/2[10\bar{1}]$.

Since the specimen was tilted to different orientations to achieve specific diffraction conditions, the images in Fig. 6 represent projections of the dislocations from six different perspectives. They thus provide valuable 3-dimensional information, allowing the determination of the dislocation line directions and the residing planes using stereological analysis. The observed dislocations were approximated as straight lines and the determined line direction $\boldsymbol{\xi}$ and line length *L* are listed in Table 2. Moreover, the dislocation character, described using the angle between the Burgers vector and line direction acos($\boldsymbol{\xi}\cdot\boldsymbol{b}$), and slip plane normal, $\boldsymbol{\xi} \times \boldsymbol{b}$, are also calculated. Examination of the $\boldsymbol{\xi} \times \boldsymbol{b}$ vectors reveals that most of the calculated planes are not exactly the {111} type slip planes in FCC crystal, except for dislocation *c* where $\boldsymbol{\xi} \times \boldsymbol{b} = [-0.57,\ -0.59,\ -0.57] \approx [111]$ and dislocation *e* where $\boldsymbol{\xi} \times \boldsymbol{b} = [-0.58,\ 0.57,\ -0.57] \approx [1\bar{1}1]$. Since they are the planes that contain both the Burgers vector and line direction, dislocation *c* and *e* are glissile. To determine the actual plane that other dislocations reside on, the deviations (δ) of the line directions $\boldsymbol{\xi}$ from the four {111} planes are calculated. Acknowledging the fact that dislocations *a, b* and *d* are glissile as suggested by their slightly curved morphology in Fig. 6, only the δ values for the permissible slip plane are listed for each segment, and the plane that is closer to the line direction (smaller absolute value of δ) is determined to be the actual slip plane. As listed in Table 2, there is no ambiguity in determining the plane with smaller deviation for most segments, because one of the δ values is much larger than the other. The line directions appear to deviate from the exact {111} planes by various values, as large as 7.5°.

With the quantitatively determined dislocation line directions and lengths, and their residing glide planes, the observed dislocation structure can be reconstructed and then projected along any direction for further examination. Fig. 7 presents the projected views of the reconstruction along four different beam directions and the comparison between the corresponding TEM images. Note that the curved dislocations *b* and *d* are represented by straight dislocation lines, the overall direction should be examined. The close alignment between the projected lines and the observed lines verifies the accuracy of the reconstruction. To explore the possible reactions between the dislocations, it is convenient to express the dislocations in terms of their respective Burgers vector and plane using the Schmid–Boas notation, namely dislocation *a* is $1/2[011](1\bar{1}1) = D1$, dislocation *b* is $1/2[110](1\bar{1}1) = D6$, dislocation *c* is $1/2[10\bar{1}](111) = B4$, dislocation *d* is $1/2[110](1\bar{1}\bar{1}) = A6$, and dislocation *e* is $1/2[011](1\bar{1}1) = D1$. As shown in Fig. 7(E), a total of three coplanar Burgers vectors and three planes are involved in this five-segment dislocation structure.

3.3. Deducing the origin of the observed structure

An important feature of the experimentally determined structure is that all five dislocation segments reside on their respective glide plane, implying that either they were directly formed on the current plane or they were formed on a different plane and subsequently cross-slipped to the current plane. In both cases, glissile reaction products must have occurred such that the resultant dislocation is glissile. According to the classical definition of a glissile reaction, two dislocations gliding on two inclined planes (α and β) intersect and form a junction which is a glissile dislocation, i.e. $\boldsymbol{b}_1^{\alpha} + \boldsymbol{b}_2^{\beta} = \boldsymbol{b}_3^{\beta}$ with the plane β containing all three Burgers vectors. For the three Burgers vectors determined and depicted on the Thompson tetrahedron in Fig. 8(A), the possible non-planar reactions leading to glissile products are $D1 + B4 = D6$, $D1 + A6 = D4$, $B4 + D6 = D1$ and $D4 + A6 = D1$.

At node 1, two dislocation segments are on the common plane *D*, and the line direction of segment *b* (*D6*) is very close to the intersection line of the planes *D* and *B* marked as a dashed green line (corresponding to $[10\bar{1}]$ (Table 2)). Therefore, the node could be readily formed by the glissile reaction of $D1 + B4 = D6$, followed by the glide of the dislocation section *b* (*D6*) by a small distance away from the intersection line of the two planes (Fig. 8(B)). At node 2, the three segments are on three planes, and none of them are close to any of the intersection lines of the planes. These details enable the following possible formation sequences to be hypothesized. One option is that node 2 could be formed by a glissile reaction, followed by the cross-slip of one segment. As demonstrated in Fig. 8(C), the dislocation segment *D6* was firstly formed by the glissile reaction between *D1* and *B4*, with an initial line direction parallel to the intersection line of the planes *B* and *D*. After bowing out, as indicated by the arrow on plane D, it underwent cross-slip from plane *D* to plane *A*, via the intersection line of the two planes, ultimately resulting in *A6*. Another option is that following the glissile reaction of $D1 + B4 = D6$, if another dislocation *A6* glides toward *D6* (Fig. 8(D)), a collinear reaction would occur, because they have the same Burgers vectors. The products are two dislocations, each residing on two planes, denoted as ($A6 + D6$). One product would continue to glide, while the other product is connected to the glissile reaction node. Subsequent gliding of *B4* and *D1* on their respective plane would produce a tri-planar configuration, forming a pinned node joined by *B4, D1* and *A6*. To summarize, the above analyses shed light on a variety of structures comprising glissile reactions beyond what has been previously envisioned, such as the classical structure in Fig. 1. What is intriguing is that the dislocation products from a glissile reaction can not only glide away from the intersection line of the participating planes, but also can evolve to a tri-planar configuration by cross-slip or subsequent collinear reaction.

Table 1
The $\boldsymbol{g}\cdot\boldsymbol{b}$ table of the diffraction vectors in Fig. 6. The Burgers vectors of the dislocations of interest are b1, b4 and b6.

		ZA	[101]			[100]		
Burgers vector		G	g_1, (020)	g_2, ($\bar{1}$11)	g_3, (11$\bar{1}$)	g_4, (002)	g_5, (022)	g_6, (02$\bar{2}$)
b1	1/2 [011]		1	1	0	1	2	0
b2	1/2[0$\bar{1}$1]		−1	0	−1	1	0	−2
b3	1/2[101]		0	0	0	1	1	−1
b4	1/2[10$\bar{1}$]		0	−1	1	−1	−1	1
b5	1/2[1$\bar{1}$0]		−1	−1	0	0	−1	−1
b6	1/2[110]		1	0	1	0	1	1

Table 2
Results of the line direction determination. The deviation of the line direction from the {111} type slip planes is calculated. The expected slip plane for each dislocation is highlighted by the angular value that is underlined.

	L (nm)	ξ			Acos($\xi \cdot b$)(°)	$\xi \times b$			Deviation of ξ from {111} planes δ(°)			
									$(1\bar{1}1)$	$(1\bar{1}\bar{1})$	$(\bar{1}\bar{1}1)$	(111)
b	447.0	[−0.68	−0.09	0.73]	57.3	[0.62	−0.62	0.49]	4.8	−49.6		
c	90.2	[−0.76	0.64	0.11]	128.3	[−0.57	−0.59	−0.57]	−48.0			−0.4
d	844.8	[−0.14	0.49	−0.86]	104.2	[−0.63	0.63	0.46]	−59.5	7.5		
a	643.8	[−0.40	0.35	0.84]	32.1	[−0.65	0.54	−0.54]	2.8		31.0	
e	559.7	[−0.18	0.60	0.78]	12.6	[−0.58	0.57	−0.57]	0.1		11.9	

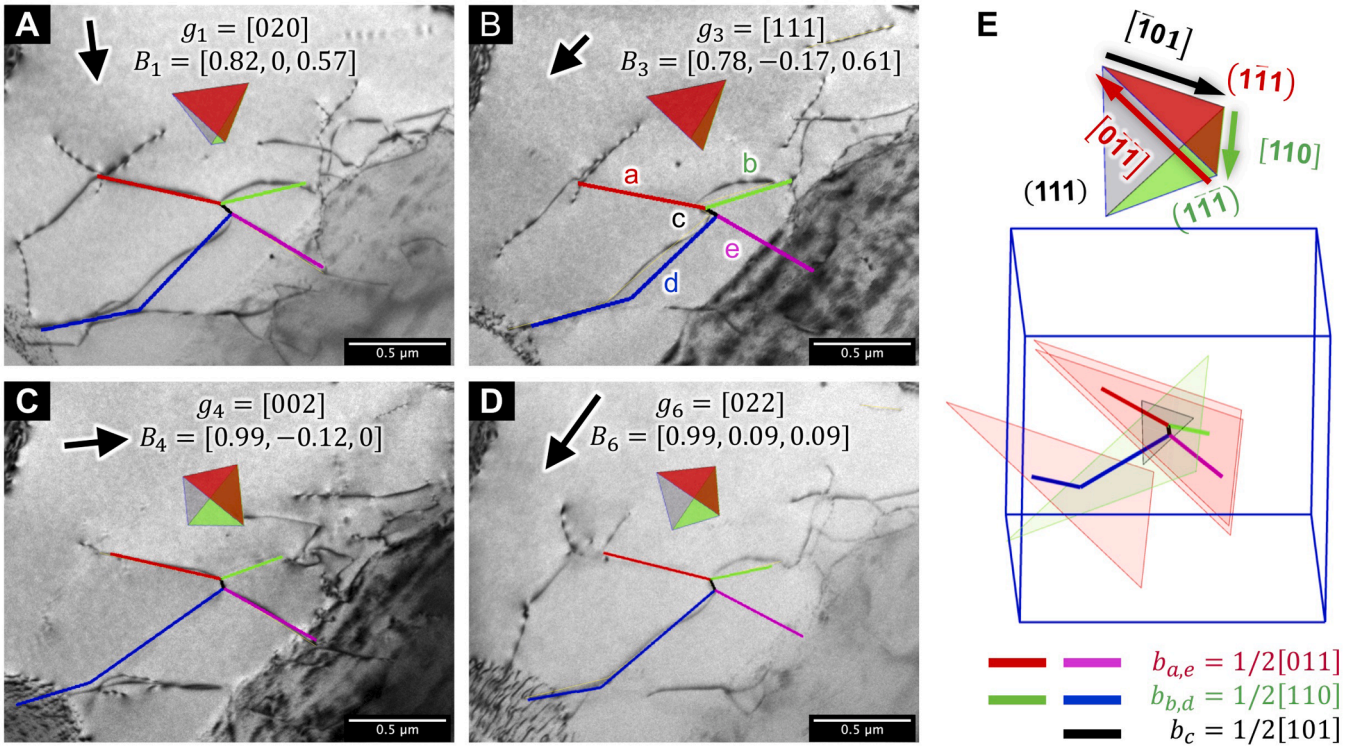

Fig. 7. (A–D) The reconstructed dislocation lines according to the results in Table 2 projected along the four beam directions and overlaid on the respective TEM images. The beam directions and diffraction vectors are annotated in each image, with the black arrow indicating the diffraction vector. (E) The dislocation structure in the cubic lattice. The crystal orientations are depicted using the colored tetrahedra.

3.4. Evolution of the structure to elucidate effective node mobility

We next investigate the mobility of the dislocations and the junction nodes, which underpin the efficacy of such structures in promoting strengthening and dislocation density via multiplication. While the individual dislocation segments formed by a glissile reaction are crystallographically mobile, the junction nodes may either be mobile or pinned due to their topology. Node 1 is shared by three dislocations, among them two co-planar segments and the third segment residing on another slip plane. In the simplest perspective, node 1 is mobile along the intersection line of the two slip planes D and B, i.e. having one degree of freedom. Node 2 is the unique intersection point of three planes, thus it has zero degrees of freedom and is in a pinned state.

To fully evaluate the possible evolution pathways in a parametric manner, we transferred the experimentally-characterized dislocation structure to a DDD simulation program DDLab [24], and applied uniaxial loads to the simulation box. Since the peripheral dislocation nodes are either connected to other dislocations or at grain boundaries as shown in Fig. 6, they are simplified as pinned nodes in the simulation. Uniaxial load was applied along different crystallographic directions, including $[\bar{1}11]$, [211], [010], $[\bar{1}\bar{1}2]$ and [213]. These directions represent cases where one or two of the slip systems is unstressed (Table 3), i.e. zero Schmid factor on the branching dislocations a and e ($[\bar{1}11]$ loading), or d ([211] loading), and the junction dislocation c ([010] loading). Obviously, the mobility of the two dislocation nodes is sensitive to the loading condition. Especially for node 2 which is at a tri-planar pinned state, whether the joining dislocations are stressed to glide would determine the evolution of the node.

Three representative scenarios are presented in Fig. 9. They demonstrate the breadth of topological evolution that can be activated in an actual microstructure, showing how defect structure and loading orientation are intimately coupled to plastic hardening. Under tensile loading along the $[\bar{1}11]$ direction (Fig. 9(A)), node 1 is mobile and node 2 is pinned. Dislocation *D1* experiences zero resolved shear stress (RSS), and the gliding of dislocation *D6* results in zipping/junction formation of the two dislocations, along the line direction of dislocation *D1:* the two co-planar dislocations react (*D6* + *D1* = *D4*) and form a third glissile dislocation on the same plane between the original node 1 and the newly formed node 3. Node 3 is thus expected to move freely on plane D, driven by the gliding of any of the attached three co-planar dislocations. On the other hand, node 2 is observed to remain in the pinned state. Notably, if the other two joining dislocations, A6 and B4, were to react, the product would be an immobile Lomer lock. The evolved configuration shown in

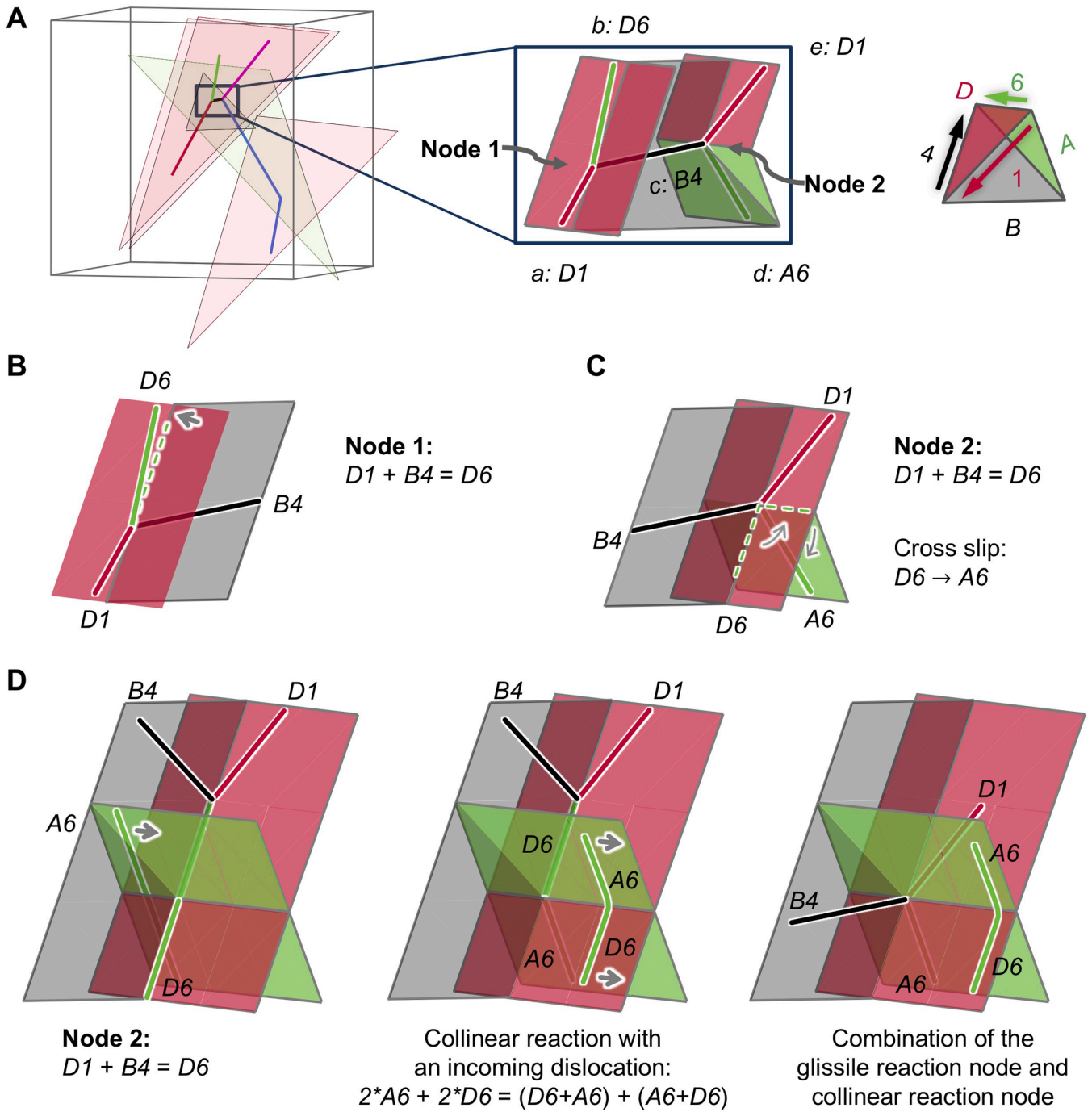

Fig. 8. (A) A closer view of the reconstructed structure. The lattice orientation and the color code for the {111} planes and 1/2⟨110⟩ Burgers vectors are shown by the tetrahedron. The planes and Burgers vectors are expressed according to the Schmid Boas notation, also shown on the tetrahedron. The possible glissile reactions and the subsequent evolution to the observed structure in (A) are presented in (B) for node 1, and in (C) and (D) for node 2.

Fig. 9(A) can thus be considered as a two degrees of freedom reaction, with the free motion of node 3 allowed on a plane.

Changing the tensile loading axis to the $[\overline{1}12]$ direction (Fig. 9(B)) results in both nodes exhibiting mobility. Dislocations *D1* and *D6* glide in opposite directions on plane *D*, so they do not zip together as in the previous scenario. Moreover, since dislocation *B4* experiences zero RSS, the movement of node 1 is constrained by the three joining dislocations to move along the intersection line of the planes *D* and *B*. At node 2, initially in a pinned state, dislocations *D1* and *A6* are stressed to glide on their respective planes thus rotating around node 2, with their gliding directions pointing to the intersection line of the two slip planes. The two dislocations subsequently zip together and produce a new segment *D4* via the glissile reaction of $D1 + A6 = D4$. The consequence of this reaction is twofold. First, the reaction occurs between node 2 and the newly formed node 3, which is shared by the mobile dislocations *D1, D4* and *A6* on two planes. Node 3 is therefore mobile but constrained to glide along the intersection line of the glide planes A and D. Second, once the new dislocation segment D4 between node 2 and node 3 is formed, node 2 changes its state to "mobile" but is constrained to move along the intersection line of the glide planes *B* and *D*. More significantly, the movement of node 2 and node 1 drags dislocation *B4* to glide under dislocation line tension, i.e. the unstressed dislocation is

Table 3
The Schmid factors of the relevant slip systems of the experimentally observed dislocation structure for different load axes, and the apparent mobility of the two dislocation nodes in the DDD simulation under tension loading. M and P represent mobile and pinned, respectively.

Load axis	Slip systems						Node mobility	
	C1	*D1*	*D6*	*A6*	*D4*	*B4*	Node 1	Node 2
$[\bar{1}\bar{1}1]$	0	0	0.27	0.27	0.27	0.27	M	P
[211]	0.27	0.27	0.41	0	0.14	0.27	M	P
[010]	0.41	0.41	0.41	0.41	0	0	M	M
$[\bar{1}\bar{1}2]$	0.27	0.14	0.27	0.27	0.41	0	M	M
[213]	0	0.47	0.35	0.18	0.12	0.18	M	M

activated. Compared with the loading condition in Fig. 9(A), this configuration has only one degree of freedom; namely, linear motion along the intersection line of two planes.

When the loading direction is reversed to compression along $[\bar{1}\bar{1}2]$ (Fig. 9(C)), both dislocation nodes are effectively immobile within the simulation steps. All the dislocations glide in the opposite directions compared to those identified during $[\bar{1}\bar{1}2]$-tensile loading. Node 1, though crystallographically mobile, is effectively immobile due to the force balance between the three joining dislocations. At node 2, dislocations *A6* and *D1* tend to induce unzipping at the node. However, since the node is pinned at the unique tri-planar point, unzipping cannot proceed, thereby leading to fundamentally distinct configurations between tensile and compressive loading. Comparatively, this configuration is the most restrictive with zero degrees of freedom. These collective results demonstrate the strong influence of the loading conditions and orientation, and highlight that, unlike individual dislocations, the ability of dislocation junctions and nodes to move is linked to the mobility of all the joining dislocation segments, which act either cooperatively to glide or to render the dislocations effectively immobile.

3.5. Statistical analysis of the mobility of the glissile reaction nodes

The parameterized DDD simulations reveal that the mobilities of the dislocations and the nodes are closely tied to each other, and the evolution of the collective dislocation network is strongly dependent on the local stress conditions. On one hand, the simple glissile nature and the cross-slip ability of individual dislocations exactly determine whether a node evolves to a pinned state, here a tri-planar point. On the other hand, remobilization of the node would evidently benefit from cross-slip of the joining dislocations. The subsequent reactions of the glissile

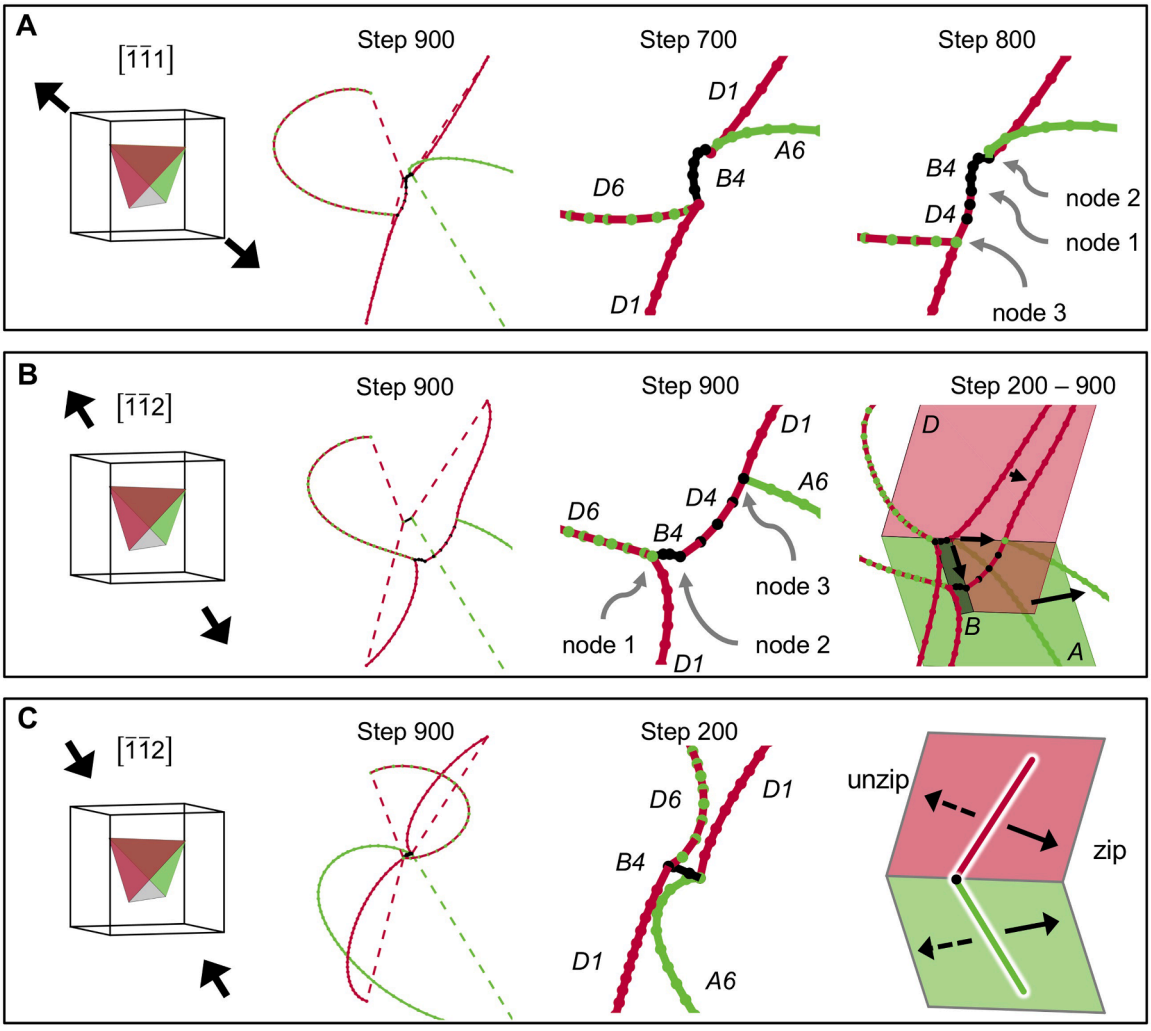

Fig. 9. DDD simulations of the evolution of the experimentally determined dislocation structure under various loading conditions. (A) tension along $[\bar{1}\bar{1}1]$ direction, (B) tension along $[\bar{1}\bar{1}2]$ direction, and (C) compression along $[\bar{1}\bar{1}2]$ direction. For each loading condition, the evolved structure at the simulation step of 900 is presented, with the original structure shown by dashed lines. Magnified views around the two nodes are shown to highlight the evolution of the dislocation lines at selected simulation steps. For each dislocation line, the line color indicates its slip plane and the node color indicates its Burgers vector. The color scheme and the Schmid Boas notations are the same as those in Fig. 8.

reaction products with other gliding dislocations could also change the mobility of the nodes. Collinear reactions could produce a pinned tri-planar configuration as depicted in Fig. 8(D). Further, co-planar reactions appear to effectively mobilize a node, as in the reaction of $D6 + D1 = D4$ at node 1 (Fig. 9(A)), which produces a mobile co-planar three-dislocation configuration.

To generalize the findings revealed by the specific dislocation structure characterized experimentally, we employed a large ensemble of dislocations in a 5 μm^3 simulation box to analyze the occurrence of glissile reactions and the evolution of the associated nodes under load, using a DDD simulation framework that has been validated on several metallic systems [3,26-30] and has unraveled dislocation multiplication mechanisms based on glissile reactions. Acknowledging the rich variety of the evolved structures, we performed tension loading simulations along the directions of [100] and [123] respectively to represent multi-slip and single-slip orientations, and also by intentionally enabling and disabling the cross-slip activity. All the simulations start from the same relaxed microstructure. The stress-strain curves for the tension simulations along the two directions, and with or without cross-slip are shown in the Appendix. It is noted that such stress-strain curves are informative of the evolution of dislocation network in a single crystal. Besides the evolution of dislocation density with strain, the following features were tracked and analyzed: (*i*) the number of glissile reactions, and (*ii*) whether a node created by a glissile reaction is pinned or mobile. Informed by the current experimentally observed structure and its evolution in DDD simulations, all the nodes that are joined by three glissile dislocations (or triple nodes) are defined as a glissile reaction node and tracked, without discriminating their origins. The other end-node of a glissile junction is excluded if this end-node is shared with Lomer or Hirth reactions. In the simulated structures, all these nodes are end-nodes of glissile junctions. The three dislocations could be bi-planar (the classical definition $\boldsymbol{b}_1^\alpha + \boldsymbol{b}_2^\beta = \boldsymbol{b}_3^\beta$), co-planar (node 3 in Fig. 9(A)), or tri-planar (node 2 in Fig. 8). We emphasize that this is a feature allowing to confirm a glissile junction and hence acts as the identification criterion.

As shown in Fig. 10, cross-slip brings a more rapid increase in dislocation density with strain, and also more rapid increase of triple nodes, i.e. the occurrence of glissile reactions. Regarding dislocation density (Fig. 10(A) and (B)), the increase is much stronger for [100] loading than for [123] loading for a given strain. The origin is likely the frequency of dislocation intersections, which is lower for single slip during [123] loading as dislocation slip and multiplication are mainly on the primary slip system. On the other hand, when examining the increase of dislocation density due to glissile reactions, it is clear that cross slip promotes glissile reactions, more than it does for other reactions. The change of dislocation density based on other mechanisms is weakly affected with or without cross-slip, while the dislocation density due to glissile reactions rises more rapidly when cross-slip is enabled.

While the evolution of dislocation density is a reflection of the enhancement effect of cross-slip on glissile reactions, the statistics of the nodes connected to three glissile dislocations (i.e. triple nodes) allows one to examine both the occurrence of glissile reactions and the mobility

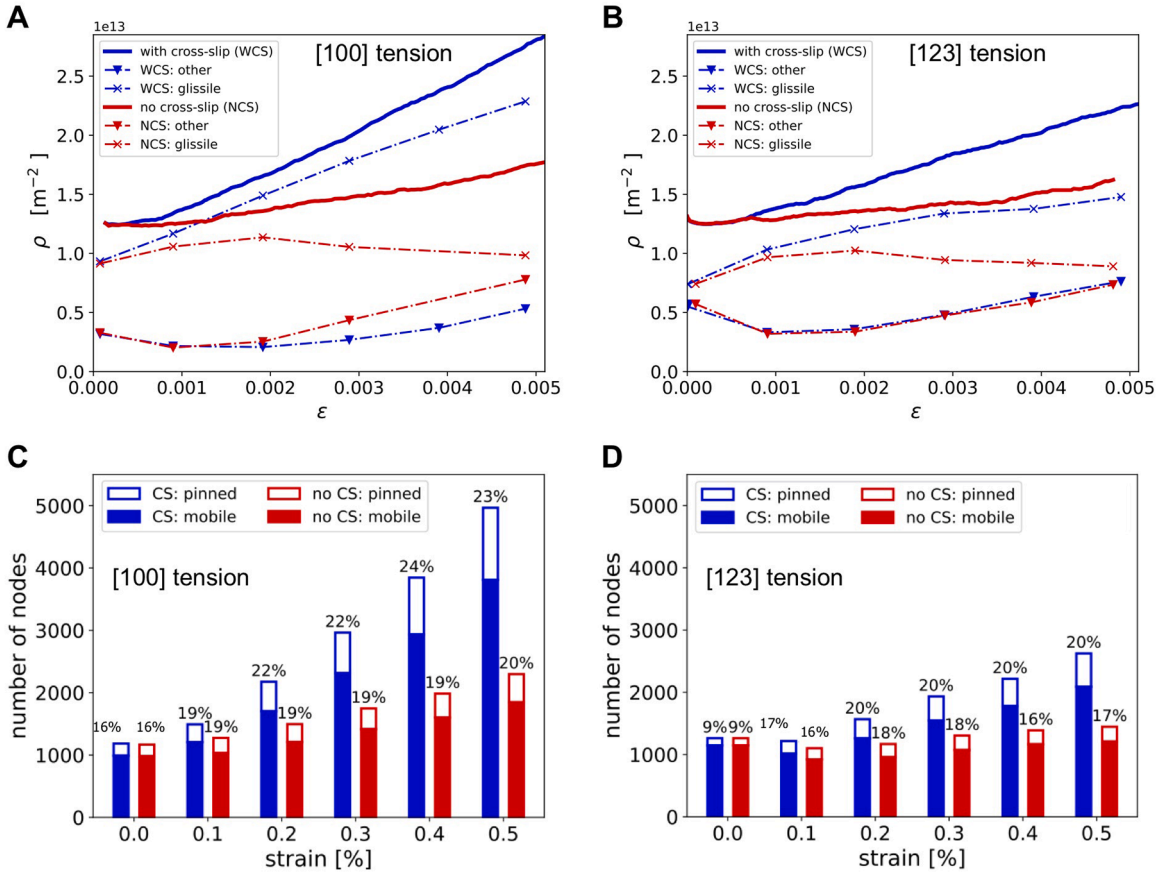

Fig. 10. The dislocation density evolution (A and B) and the evolution of the number of dislocation nodes joined by glissile dislocations (C and D) with total strain. (A) and (C) are obtained under [100] tension, and (B) and (D) are obtained under [123] tension. For both loading directions, simulation with and without cross-slip are shown. In (A) and (B), the total dislocations are separated from those due to glissile reaction and other dislocations. Namely, for either with cross-slip (WCS) or with no cross-slip (NCS), the curves with triangular markers represent the dislocation density produced by glissile reaction, the curves with cross markers represent the dislocation density evolution of other dislocations (e.g. produced by other reactions), and the solid line curves are the total dislocation density. The fraction of pinned nodes is indicated above each bar in (C) and (D). The simulations were performed using DDD with 1.15×10^{13} m^{-2} starting dislocation density in a 125 μm^3 simulation box.

of the resulting nodes. For both the [100] and [123] tensile loading simulations, cross-slip results in more nodes of glissile reactions. The orientation dependence of this enhancement factor is unknown and worthy of future study. Consistent with the above simulations on the specific structure, both pinned and mobile nodes are found among the triple nodes. The fraction of immobile pinned nodes can be as high as 20 % at 0.5 % strain, a surprising observation considering all the joining dislocations are glissile on their own planes. The fraction of the pinned nodes is slightly higher when cross-slip is enabled than when not. This is due to the additional relaxation by cross-slip that allows the formation of stable yet pinned triple nodes. Overall, the statistics suggest that cross-slip is an important mechanism to initiate more glissile reactions and generate more mobile dislocation nodes.

3.6. Implications for crystal plasticity modeling

The statistical analyses of glissile reactions and the mobility of the resulting nodes uncover new understandings on the implications of glissile reactions on plasticity. The duality of node mobility emphasizes the role of glissile reactions in both providing mobile dislocations as carriers of plastic strain and producing immobile structures as obstacles for dislocation movement. In the two extreme cases, a structure produced by a glissile reaction could move freely by the glide of all the branching dislocations and the corresponding nodes, or it could include nodes with zero effective mobility that act as pinning sites.

The current study reveals that the apparent mobility of the reaction node or the dislocations differs for materials of different SF energy (or the properly normalized global metric γ_{SF}/μ [36]) and the ability to cross-slip, at minimum. As shown in the MD simulations in Fig. 5, the apparent mobility of glissile reaction nodes of Cu, a low SFE representative, is much lower than that of Al, a high SFE representative. This is partly due to the larger length of the sessile stair-rod partial dislocation in Cu than in Al, as an intermediate product of the sequential reactions of partial dislocations. While SF energy could be considered as an intrinsic property of a material, extrinsic factors, such as stress state, strain rate [37] and grain size [38], would also affect the propensity for cross-slip. Both the parametric DDD simulations in Fig. 9 and the statistical analysis of the DDD simulation in Fig. 10 suggests that loading conditions and activity of different slip systems would significantly affect the mobility of the glissile reaction node.

The generation and activation of mobile dislocations, as a result of glissile reaction, would readily dissipate strain energy, especially the activation of unstressed dislocations that are dragged by a mobile node (dislocation *B4* in Fig. 9(B)), i.e. zero resolved shear stress but non-zero plastic strain rate. In this regard, they contribute to homogeneous deformation and the relaxation of internal elastic stress, in contrast to the increased hardening brought about by dislocation locks. In recent years, there have already been endeavors in implementing glissile reactions in dislocation density-based crystal plasticity models, with the goal of achieving physically meaningful descriptions of hardening [39–41]. The results presented here suggest that the dual nature of node mobility could be further implemented in such formulations. For instance, a first step could be assigning a certain fraction of glissile reaction nodes as immobile nodes, with the value informed by DDD simulations such as in Fig. 10(B), analogous to informing the hardening matrix using the values obtained by pair-wise dislocation interaction simulations [42,43]. Taken collectively, this work encourages future modeling efforts on both the discrete dislocation scale and the continuum scale that would treat the mobility of the resulting dislocations in a statistical and evolving sense.

4. Conclusions

In summary, we elucidated the glissile reaction pathway and evolution using MD simulations, demonstrating its natural occurrence for dissociated partial dislocations and also the dependence of reaction node mobility on SF energy, thereby extending the current understandings of glissile reactions based primarily on perfect dislocations. A dislocation structure produced by glissile reactions was then quantitatively characterized experimentally, and recapitulated in parametric discrete dislocation dynamics simulations to systematically interrogate the complex and myriad evolutions of this experimentally-determined structure. In-depth analyses of the specific dislocations in tandem with a statistical analysis of an ensemble of dislocations reveal the multiplicity of the structures evolving from glissile reaction, the duality of the mobility of the dislocations and nodes, and their implications on plasticity. These findings provide crucial ingredients for the development of physically-informed, dislocation-based constitutive theories of plasticity [44–47], and further point to avenues for tailoring plastic response through alloy and microstructure design.

Declaration of competing interest

The authors declare that they have no known competing financial interests or personal relationships that could have appeared to influence the work reported in this paper.

Acknowledgments

This work is partly funded by Shanghai Pujiang Program (No. 21PJ1406700) and National Natural Science Foundation of China (No. 52071211). D.W. acknowledges funding by the German Research Foundation (DFG) under Contract number WE 3544/7-1. D.C. acknowledges financial support from the National Natural Science Foundation of China (No. 12272224). This work employed the MRL Shared Experimental Facilities at UC Santa Barbara, which are supported by the MRSEC Program of the NSF under Award no. DMR 1720256; a member of the NSF-funded Materials Research Facilities Network (www.mrfn.org). This work was sponsored by the Army Research Office under Grant number W911NF-21-1-0288. The views and conclusions contained in this document are those of the authors and should not be interpreted as representing the official policies, either expressed or implied, of the Army Research Office or the U.S. Government. The U.S. Government is authorized to reproduce and distribute reprints for Government purposes notwithstanding any copyright notation herein.

Appendix

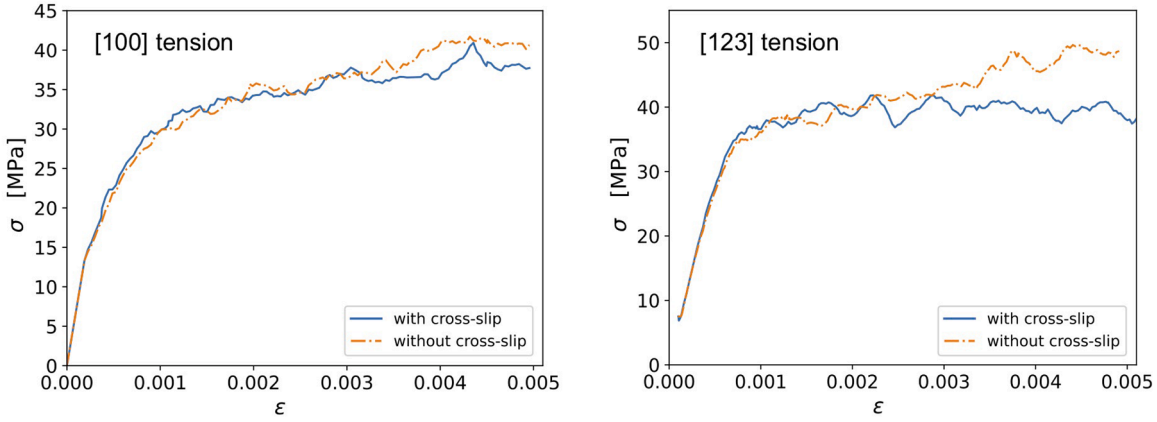

Fig. A1. The stress-strain curves for [100] and [123] tensile loadings respective. In each case, the curves for the simulations with and without cross-slip are shown.

The primary purpose of the stress-strain curves (Fig. A1) of the large scale DDD simulations is to examine the general elastic and plastic response of the simulation box, including reasonable yielding behavior and level of flow stress etc., with the used cross-slip model and parameters. Cross-slip is shown to reduce strain hardening, and in both loading cases, the simple proportionality between flow stress and the square root of dislocation density does not hold. One possible origin of this observation is attributed to the cuboidal shape of the simulation volume and the chosen displacement boundary conditions, which enforce the top and bottom surface to be overall flat. While the dislocation density is quite large (the average spacing between dislocations is significantly smaller than sample size), underneath the top and bottom surface of the sample, back stresses on the dislocations exist and cross-slip allows for an additional relaxation, leading to lower stresses with increasing strain. This is more clearly visible for the [123] loading case (single slip) as the primary slip system is steeper and thus geometrically more constrained by boundary constraints.

References

[1] P. Anderson, J. Hirth, J. Lothe, Theory of Dislocations, Cambridge University Press, Cambridge, 2017.
[2] R. Madec, B. Devincre, L. Kubin, T. Hoc, D. Rodney, The role of collinear interaction in dislocation-induced hardening, Science 301 (2003) 1879–1882.
[3] M. Stricker, D. Weygand, Dislocation multiplication mechanisms—Glissile junctions and their role on the plastic deformation at the microscale, Acta Mater. 99 (2015) 130–139.
[4] M. Stricker, M. Sudmanns, K. Schulz, T. Hochrainer, D. Weygand, Dislocation multiplication in stage II deformation of fcc multi-slip single crystals, J. Mech. Phys. Solids 119 (2018) 319–333.
[5] S. Akhondzadeh, N. Bertin, R. Sills, W. Cai, Slip-free multiplication and complexity of dislocation networks in FCC metals, Mater. Theory 5 (2021) 2.
[6] R. Sills, N. Berin, A. Aghaei, W. Cai, Dislocation networks and the microstructural origin of strain hardening, Phys. Rev. Lett. 121 (2018) 085501.
[7] L. Kubin, R. Madec and B. Devincre, "in MRS symposium proceedings, edited by H. Zbit, D. Lassila, L. Levine, and K. Hemker (Materials Research Society, Warrendale, 2003)," 779, 25–26.
[8] F. Roters, M. Diehl, P. Shanthraj, et al., DAMASK—The Düsseldorf advanced material simulation kit for modeling multi-physics crystal plasticity, thermal, and damage phenomena from the single crystal up to the component scale, Comput. Mater. Sci. 158 (2019) 420–478.
[9] M.J. Whelan, N.F. Mott, Dislocation interactions in face-centred cubic metals, with particular reference to stainless steel, Proc. R. Soc. Lond. Ser. A Math. Phys. Sci. 249 (1959) 114–137.
[10] R. Madec, L. Kubin, Dislocation strengthening in FCC metals and in BCC metals at high temperatures, Acta Mater. 126 (2017) 166–173.
[11] J. Han, S. Thomas, D. Srolovitz, Grain-boundary kinetics: a unified approach, Prog. Mater. Sci. 98 (2018) 386–476.
[12] S. Thomas, C. Wei, J. Han, Y. Xiang, D. Srolovitz, Disconnection description of triple-junction motion, Proc. Natl. Acad. Sci. 116 (2019) 8756–8765.
[13] S. Plimpton, Fast parallel algorithms for short-range molecular dynamics, J. Comput. Phys. 117 (1995) 1–19.
[14] Y. Mishin, Structural stability and lattice defects in copper: ab initio, tight-binding, and embedded-atom calculations, Phys. Rev. B 63 (2001) 224106.
[15] J.E. Angelo, N.R. Moody, M.I. Baskes, Trapping of hydrogen to lattice defects in nickel, Model. Simul. Mater. Sci. Eng. 3 (1995) 289–307.
[16] A. Stukowski, Visualization and analysis of atomistic simulation data with OVITO–the open visualization tool, Model. Simul. Mater. Sci. Eng. 18 (2010) 015012.
[17] J. Kacher, I. Robertson, In situ and tomographic analysis of dislocation/grain boundary interactions in α-titanium, Philos. Mag. 94 (2014) 814–829.
[18] J. Kacher, G. Liu, I. Robertson, Visualization of grain boundary/dislocation interactions using tomographic reconstructions, Scr. Mater. 64 (2011) 677–680.
[19] G. Liu, S. House, J. Kacher, M. Tanaka, K. Higashida, I. Robertson, Electron tomography of dislocation structures, Mater. Charact. 87 (2014) 1–11.
[20] A. Dlouhy, G. Eggeler, Superdislocation line directions in gamma'-particles after double shear creep of superalloy single crystals, Prakt. Mettallogr. 33 (1996) 12.
[21] R. McCabe, A. Misra, T. Mitchell, K. Alexander, A single-tilt TEM stereomicroscopy technique for crystalline materials, Microsc. Microanal. 9 (2003) 29–35.
[22] J. Edington, Practical Electron Microscopy in Materials Science, Van Nostrand Reinhold Co, New York, 1976.
[23] F. Wang, G. Balbus, S. Xu, Y. Su, J. Shin, P. Rottmann, K. Knipling, J. Stinville, L. Mills, O. Senkov, I. Beyerlein, T. Pollock, D. Gianola, Multiplicity of dislocation pathways in a refractory multiprincipal element alloy, Science 370 (2020) 95–101.
[24] W. Cai, A. Arsenlis, C. Weinberger, V. Bulatov, A non-singular continuum theory of dislocations, J. Mech. Phys Solids 54 (2006) 561–587.
[25] K. Davoudi, Temperature dependence of the yield strength of aluminum thin films: Multiscale modeling approach, Scr. Mater. 131 (2017) 63–66.
[26] D. Weygand, L. Friedman, E. der Giessen, A. Needleman, Aspects of boundary-value problem solutions with three-dimensional dislocation dynamics, Modell. Sinul. Mater. Sci. Eng. 10 (2002) 437–468.
[27] D. Weygand, P. Gumbsch, Study of dislocation reactions and rearrangements under different loading conditions, Mater. Sci. Eng. 400–401 (2005) 158–161.
[28] D. Weygand, J. Senger, C. Motz, W. Augustin, V. Heuveline, P. Gumbsch, High performance computing and discrete dislocation dynamics: plasticity of micrometer sized specimens, High Perform. Comput. Sci. Eng. 08 (2009) 507–523.
[29] J. Senger, D. Weygand, P. Gumbsch, O. Kraft, Discrete dislocation simulations of the plasticity of micro-pillars under uniaxial loading, Scr. Mater. 58 (2008) 587–590.
[30] T. El-Achkar, D. Weygand, Aspects on numerical integration of dislocation surface traction fields for discrete dislocation dynamics FEM coupling: the case of emerging dislocations, Model. Simul. Mater. Sci. Eng. 28 (2020) 85010.
[31] E. Van der Giessen, A. Needleman, Discrete dislocation plasticity: a simple planar model, Model. Simul. Mater. Sci. Eng. 3 (1995) 689–735.
[32] C. Motz, D. Weygand, J. Senger, P. Gumbsch, Initial dislocation structures in 3-D discrete dislocation dynamics and their influence on microscale plasticity, Acta Mater. 57 (2009) 1744–1754.
[33] M. Verdier, M. Fivel, I. Groma, Mesoscopic scale simulation of dislocation dynamics in fcc metals: Principles and applications, Model. Simul. Mater. Sci. Eng. 6 (1998) 755–770.
[34] L. Kubin, G. Canova, M. Condat, B. Devincre, V. Pontikis, Y. Brechet, Dislocation microstructures and plastic flow: a 3D simulation, Solid State Phenomena 23–24 (1992) 455–472.
[35] M. Fivel, PHD THESES INPG, 1997, Grenoble, France.
[36] P. Coulomb, Comment on graphs relating some property to stacking fault energy, Scr. Metall. 15 (1981) 769–770.
[37] Z. Wang, I. Beyerlein, R. LeSar, The importance of cross-slip in high-rate deformation, Model. Simul. Mater. Sci. Eng. 15 (2007) 675.

[38] A. Hussein, S. Rao, M. Uchic, D. Dimiduk, J. El-Awady, Microstructurally based cross-slip mechanisms and their effects on dislocation microstructure evolution in fcc crystals, Acta Mater. 85 (2015) 180–190.
[39] M. Sudmanns, M. Stricker, D. Weygand, T. Hochrainer, K. Schulz, Dislocation multiplication by cross-slip and glissile reaction in a dislocation based continuum formulation of crystal plasticity, J. Mech. Phys. Solids 132 (2019) 103695.
[40] F. Roters, M. Diehl, P. Shanthraj, P. Eisenlohr, C. Reuber, S.L. Wong, T. Maiti, A. Ebrahimi, T. Hochrainer, H.-O. Fabritius, S. Nikolov, M. Friák, N. Fujita, N. Grilli, K.G.F. Janssens, N. Jia, P.J.J. Kok, D. Ma, F. Meier, E. Werner, M. Stricker, D. Weygand, D. Raabe, DAMASK—The Düsseldorf advanced material simulation kit for modeling multi-physics crystal plasticity, thermal, and damage phenomena from the single crystal up to the component scale, Comput. Mater. Sci. 158 (2019) 420–478.
[41] Sh. Akhondzadeh, R.B. Sills, N. Bertin, W. Cai, Dislocation density-based plasticity model from massive discrete dislocation dynamics database, J. Mech. Phys. Solids 145 (2020) 104152.
[42] N. Bertin, C.N. Tome, I.J. Beyerlein, M.R. Barnett, L. Capolungo, On the strength of dislocation interactions and their effect on latent hardening in pure magnesium, Int. J. Plast. 62 (2014) 72–92.
[43] J.J. Bhattacharyya, F. Wang, P.D. Wu, W.R. Whittington, H. El Kadiri, S.R. Agnew, Demonstration of alloying, thermal activation, and latent hardening effects on quasi-static and dynamic polycrystal plasticity of Mg alloy, WE43-T5, plate, Int. J. Plast. 81 (2016) 123–151.
[44] T. Hochrainer, S. Sandfeld, M. Zaiser, P. Gumbsch, Continuum dislocation dynamics: towards a physical theory of crystal plasticity, J. Mech. Phys. Solids 63 (2014) 167–178.
[45] P. Lin, A. El-Azab, Implementation of annihilation and junction reactions in vector density-based continuum dislocation dynamics, Model. Simul. Mater. Sci. Eng. 28 (2020) 045003.
[46] B. Katzer, K. Zoller, D. Weygand, K. Schulz, Identification of dislocation reaction kinetics in complex dislocation networks for continuum modelling using data-driven methods, J. Mech. Phys. Solids 168 (2022) 105042.
[47] C. Denoual, Y. Pellegrini, P. Lafourcade, R. Madec, Dislocation storage-release-recovery model for metals under strain rates from 10^{-3} to 10^{7} s^{-1}, and application to tantalum, J. Appl. Phys. 28 (2024) 045101.